Optimal Shape Design of microfluidic devices for viscoelastic fluid flow

Manuel A. Alves

Faculdade de Engenharia da Universidade do Porto, Centro de Estudos de Fenómenos de Transporte
Departamento de Engenharia Química, Rua Dr. Roberto Frias s/n, 4200-465 Porto, Portugal
email: mmalves@fe.up.pt web: http://www.fe.up.pt

Abstract

In this work we describe an integrated algorithm for optimal shape design of viscoelastic fluid flow. For this purpose we couple a finite-volume viscoelastic code [1] with the CONDOR optimizer [2] and a fully automated mesh generation and adaptation procedure. The main goal is to find the shape of a given flow geometry, in order to achieve optimal performance. We design an optimized microfluidic extensional rheometer-on-a-chip appropriate for measuring the extensional viscosity of dilute polymeric solutions. The microfluidic device proposed consists of a cross-slot flow geometry with optimal shape, which generates a homogeneous elongational flow with regions of constant strain-rate, thus producing a purely extensional flow along the centerline, a requirement to produce meaningful rheological measurements.

Key Words: *Optimal shape design; Viscoelastic fluid flow; Cross slot; Extensional viscosity; Microfluidics.*

1 Introduction

Optimal shape design (OSD) tools can be used in a wide variety of applications, ranging from fluid mechanics to electromagnetism or structure mechanics, or even to a combination of the three [3]. As typical examples of engineering applications, OSD techniques have been used in airplane optimization [4], harbor design [5], or optimal design of rotary blood pumps for artificial hearts [6].

In order to develop optimization methods for computational fluid dynamics (CFD) studies three main components are usually necessary [7]: (*i*) a method to solve the nonlinear optimization problem, defined by an objective function and the functional constraints; (*ii*) a method for modeling the flow geometry based on the design variables, and automatically generate the mesh; (*iii*) an efficient CFD flow solver that allows the calculation of the objective function and functional constraints.

Application of CFD-based optimization tools in engineering applications is valuable, but also numerically challenging and demanding in terms of necessary computational resources. Numerical algorithms for OSD have evolved significantly in the recent past but there is still no clear indication of the best methodology to use in CFD-based applications. Descent algorithms based on gradient information are frequently used to solve the resulting nonlinear optimization problems. On the other hand, gradient-free optimization methodologies, such as genetic algorithms (GA), are also an interesting alternative. Genetic algorithms possess the ability to locate the global optimum and their implementation is straightforward. However, the computational payload is high due to the large number of objective function calculations needed, each one requiring a complete CFD simulation, thus leading to high computational times, and frequently requiring the use of parallel solvers. As a result, the computational cost is frequently prohibitive for routine industrial applications [8]. Genetic algorithm optimization strategies are currently better suited when a small number of parameters are to be optimized [9]. According to Mohammadi and Pironneau [3] the future of OSD lies most probably in the coupling of different classes of optimization methods.

In this work we will focus on the development of OSD strategies for laminar viscoelastic fluid flows. A finite-volume viscoelastic code [1] will be used, coupled with the CONDOR derivative-free optimizer [2]. A fully automated mesh generation and adaptation procedure will be developed for application in the design of an optimized cross-slot flow micro device. The selection of the CONDOR optimizer was motivated by its easy implementation and for being freely available. This derivative-free optimizer has other specific advantages for CFD-based optimization studies, such as the ability to deal with constrained and noisy objective functions. Furthermore, it was devised to minimize the number of objective functions evaluations, a desired property for CFD-based optimization studies. The algorithms used in the CONDOR optimizer are part of the Gradient-Based

optimization family [10,11]. CONDOR is essentially a generalization of Powell's UOBYQA methodology [12] capable of handling constrained optimization studies.

Automatic optimal shape design of microfluidic devices for Newtonian and viscoelastic fluids is an emerging and challenging area of research. Microfluidics refers to devices used for manipulating flows with characteristic length scales of the order of tens of micrometers [13]. These flows occur naturally under laminar, low Reynolds number flow conditions, and the ratio of surface to volume forces is usually very large [14]. The study of micro flows of complex fluids has been restricted mainly to experimental investigations [15-18], and consequently the development of microfluidic devices has been usually based on intuition and trial-and-error. The small sizes characteristic of microfluidics enhance the role of elasticity to levels far beyond those typical at the "macroscopic" scale and elastic instabilities are prone to develop even for creeping flow conditions, as illustrated in the recent experiments of Arratia et al. [19] in a microfluidic cross-slot device.

As a practical application of the OSD methodology, we will design an optimized microfluidic rheometer-on-a-chip suitable for measuring the extensional viscosity of dilute polymeric solutions. This material property is extremely difficult to measure and currently there are no commercial instruments available for dilute polymer solutions. We will focus our analysis on cross-slot devices, and will search for the *best* design in order to achieve optimal performance, which corresponds to an ideal planar extensional flow. The classical cross-slot geometry, illustrated in Figure 1(a), does not allow achieving a truly extensional flow due to the influence of the walls on the flow field [20]. Therefore, in order to achieve a truly extensional flow, we will search for the optimal shape of the cross-slot for viscoelastic fluid flow under low Reynolds number flow conditions, as sketched in Figure 1(b). We will consider the limiting case of inertialess flow conditions, which are typical of microfluidic applications. Therefore, with this work we envisage the design of an optimized cross-slot microfluidic chip, with application in the measurement of extensional viscosity of dilute polymeric solutions.

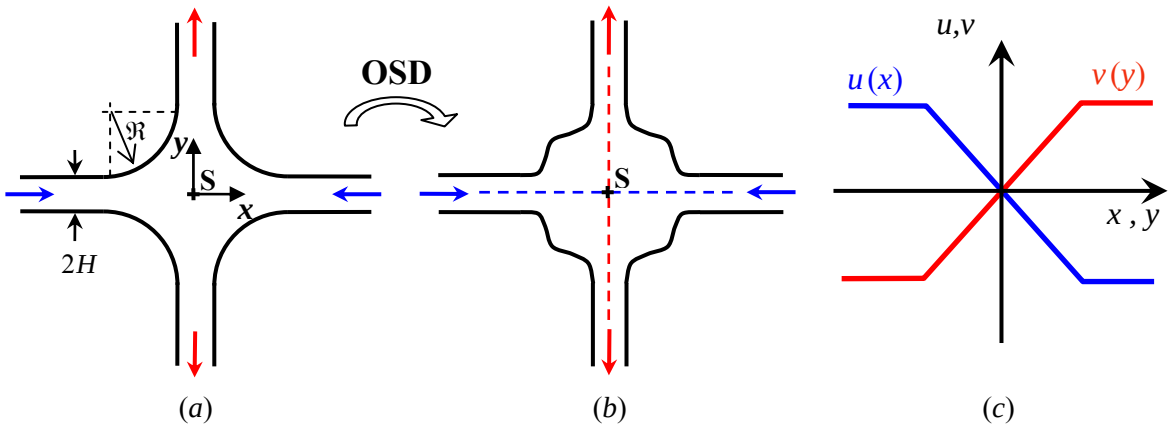

Fig.1. Illustration of (*a*) the initial flow configuration (a classical cross-slot flow geometry with rounded corners) and (*b*) the optimized flow geometry to be obtained through optimal shape design. The target velocity profiles are displayed in part (*c*), and correspond to an ideal planar extensional flow.

2 Numerical Method

2.1 Optimization cycle

The optimal shape design methodology developed in this work is composed of an automatic mesh generator program, a viscoelastic flow solver [1] and the CONDOR [2] optimizer. Based on an initial estimate of the design variables, the initial mesh is automatically generated. The flow geometry is assumed to be symmetric relative to the *x*- and *y*-axis, as depicted in Figure 1 (*a*,*b*), therefore only one quarter (the first quadrant) of the geometry is optimized, and the remaining walls are obtained assuming geometrical symmetry.

A diagram illustrating the important steps of the optimization cycle is presented in Figure 2. The initial estimate of the flow geometry is depicted in Figure 1 (*a*) and was assumed to be a cross-slot with rounded walls (with a radius of curvature, $\Re = 20H$, where H represents the half-width of the channels). From this initial estimate the mesh is automatically generated and the CFD simulation is undertaken. From the numerical solution the objective function is calculated, and this information is transferred to the CONDOR optimizer. If the minimum of the defined objective function is achieved, then the optimal shape was found, otherwise the CONDOR optimizer provides a new estimate of the design variable array, and the full cycle is repeated until the minimum value of the objective function is reached.

In the mesh generation step the shape of the flow geometry is defined in terms of the design variables, **X** (which represents an array of *N* variables to be searched by the optimization procedure). During the optimization cycle, as the solution **X** evolves towards the optimum, the boundary of the cross-slot is altered accordingly and the mesh is adjusted in order to follow the shape evolution of the boundary walls.

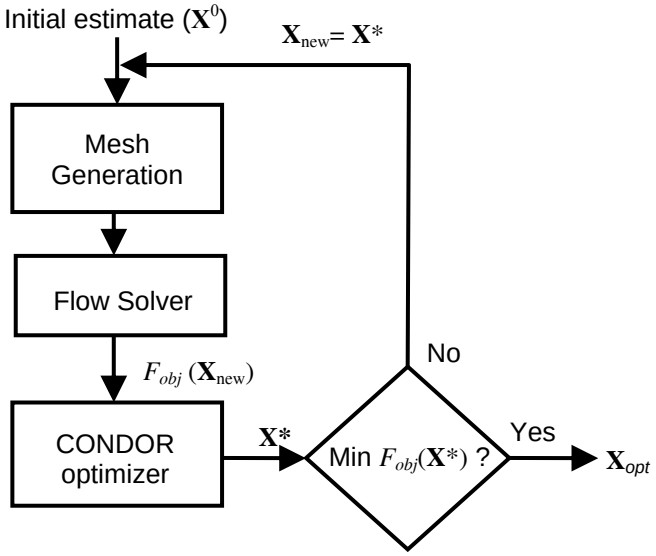

Fig.2. Schematic representation of the optimization cycle.

The objective function selected for this work was

$$F_{obj} = \sum_i \left|(u_i - u_{i,\text{target}})/u_{i,\text{target}}\right|\Delta x_i + \sum_j \left|(v_j - v_{j,\text{target}})/v_{j,\text{target}}\right|\Delta y_j \tag{1}$$

and represents the sum of the relative differences between the calculated and target streamwise velocity profiles along the horizontal and vertical center lines, $y = 0$ and $x = 0$ respectively. The minimum of this objective function is sought by the optimization algorithm.

The target velocity profiles are sketched in Figure 1 (*c*), and correspond to a constant strain-rate velocity field in the regions $-15 \le x/H \le 15$ and $-15 \le y/H \le 15$. Assuming an average velocity *U* on the inlet arms (note that on the center line the streamwise velocity is $1.5U$ under fully-developed flow conditions), the target velocity profiles are given by

$$u(x,0)/U = \begin{cases} 1.5 & x/H < -15 \\ -0.1\,x/H & -15 \le x/H \le 15 \\ -1.5 & x/H > 15 \end{cases} \qquad v(0,y)/U = \begin{cases} -1.5 & y/H < -15 \\ 0.1\,y/H & -15 \le y/H \le 15 \\ 1.5 & y/H > 15 \end{cases} \tag{2}$$

and the corresponding strain-rate ($\dot{\varepsilon}$) profiles are

$$\dot{\varepsilon}(x,0)/(U/H) = -\frac{\partial(u/U)}{\partial(x/H)} = \begin{cases} 0.1 & |x/H| \le 15 \\ 0 & |x/H| > 15 \end{cases} \qquad \dot{\varepsilon}(0,y)/(U/H) = \frac{\partial(v/U)}{\partial(y/H)} = \begin{cases} 0.1 & |y/H| \le 15 \\ 0 & |y/H| > 15 \end{cases} \tag{3}$$

which correspond to a constant strain-rate (ideal) planar extensional flow.

2.2 Flow Solver

The flow solver used in this work is a finite-volume code developed for simulation of laminar flows of viscoelastic fluids described by differential-type constitutive equations [1]. The equations we need to solve are those expressing conservation of mass

$$\nabla \cdot \mathbf{u} = 0 \tag{4}$$

and linear momentum

$$-\nabla p + \nabla \cdot \boldsymbol{\tau} = \mathbf{0} \tag{5}$$

Under creeping flow conditions, which should be coupled with an appropriate constitutive equation for the extra stress, $\boldsymbol{\tau}$. In this work, we will use the upper-convected Maxwell (UCM) model to specify $\boldsymbol{\tau}$,

$$\boldsymbol{\tau} + \lambda\left(\frac{\partial \boldsymbol{\tau}}{\partial t} + \nabla \cdot \mathbf{u}\boldsymbol{\tau}\right) = \eta\left(\nabla \mathbf{u} + \nabla \mathbf{u}^{\mathrm{T}}\right) + \lambda\left(\boldsymbol{\tau} \cdot \nabla \mathbf{u} + \nabla \mathbf{u}^{\mathrm{T}} \cdot \boldsymbol{\tau}\right) \tag{6}$$

where λ and η are the relaxation time and the shear viscosity of the fluid, respectively. The constitutive equation for a Newtonian fluid is recovered by setting $\lambda = 0$.
The details of the numerical technique have been described elsewhere [1] and therefore are not repeated here. The flow solver operates like a *black-box* in the optimization cycle.

3 Results and Discussion

In this section we will analyze the effect of the Deborah number ($De = \lambda U/H$) on the optimal shape of the optimized cross-slot geometry. In order to develop efficient microfluidic cross-slot devices for extensional viscosity measurements, the optimized shape of geometry should be insensitive to the Deborah number as much as possible.

Two meshes were used in the numerical simulations. The coarse mesh (M1) is composed of 1521 cells while the refined mesh (M2) has a total of 5825 cells. A zoomed view near the center of the rounded cross-slot, used as initial estimate, is shown in Figure 3 for both meshes.

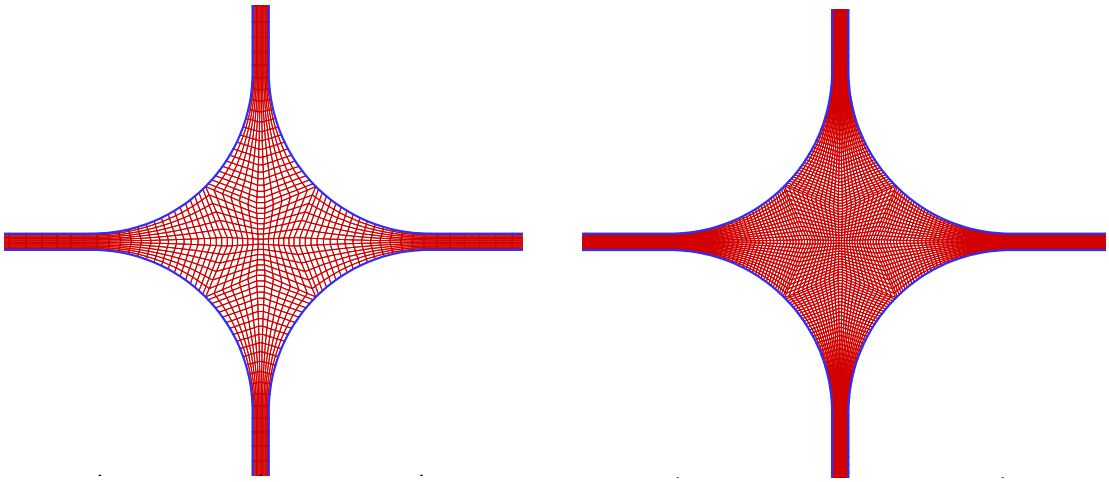

(*a*) (*b*)

Fig.3. Zoomed view of the computational meshes. (*a*) Mesh M1; (*b*) Mesh M2. The configuration represented corresponds to the initial estimate which represents a rounded cross-slot with a radius of curvature $\Re = 20H$.

The shape of the cross-slot flow geometry is described by N parameters, which are stored in a solution array, $\mathbf{X}$. The dimension of the search space, N, should not be large. The CONDOR optimizer used in this work is particularly adequate when the dimension of the search space is low ($N < 100$) [2]. In this work we will use B-splines to describe the cross-slot shape, and a total of $N = 9$ parameters will be used in most of the optimization test-cases. Figure 4 illustrates how the shape of the cross-slot is reconstructed from the knots that define the B-spline function. The points represented in blue (●) are fixed, while the points ($N = 9$) represented in green (◉) can move along the rays represented as dashed green lines in Figure 4. The distance between these knots and point A, represented in Figure 4, is the solution $\mathbf{X}$ of our problem, and these distances (X_i: $i = 1, N$) should be searched by the optimization algorithm in order to minimize the objective function described by Eq. (1). The B-spline function that defines the shape of the cross-slot geometry uses four fixed and N variable points. We note that in general the B-splines only interpolate the extreme points. The slope of the B-spline on these boundaries equals the slope of the straight line that connects the two extreme points, hence the use of the four fixed points illustrated in Figure 4 (●). These fixed points provide a smooth and continuous transition between the curved and straight walls of the cross-slot.

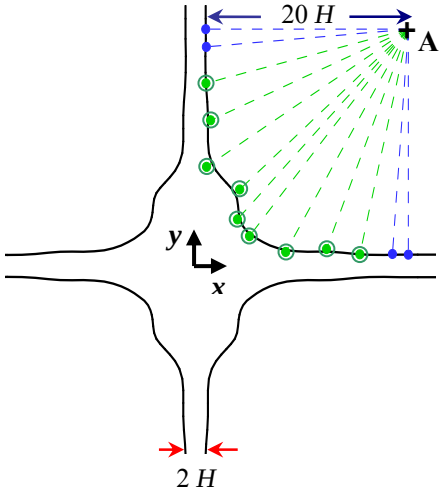

Fig.4. Reconstruction of the boundary of the cross-slot from the location of the points that define the B-spline function. The points represented in blue (●) are fixed, while the points represented in green (◉) are adjustable.

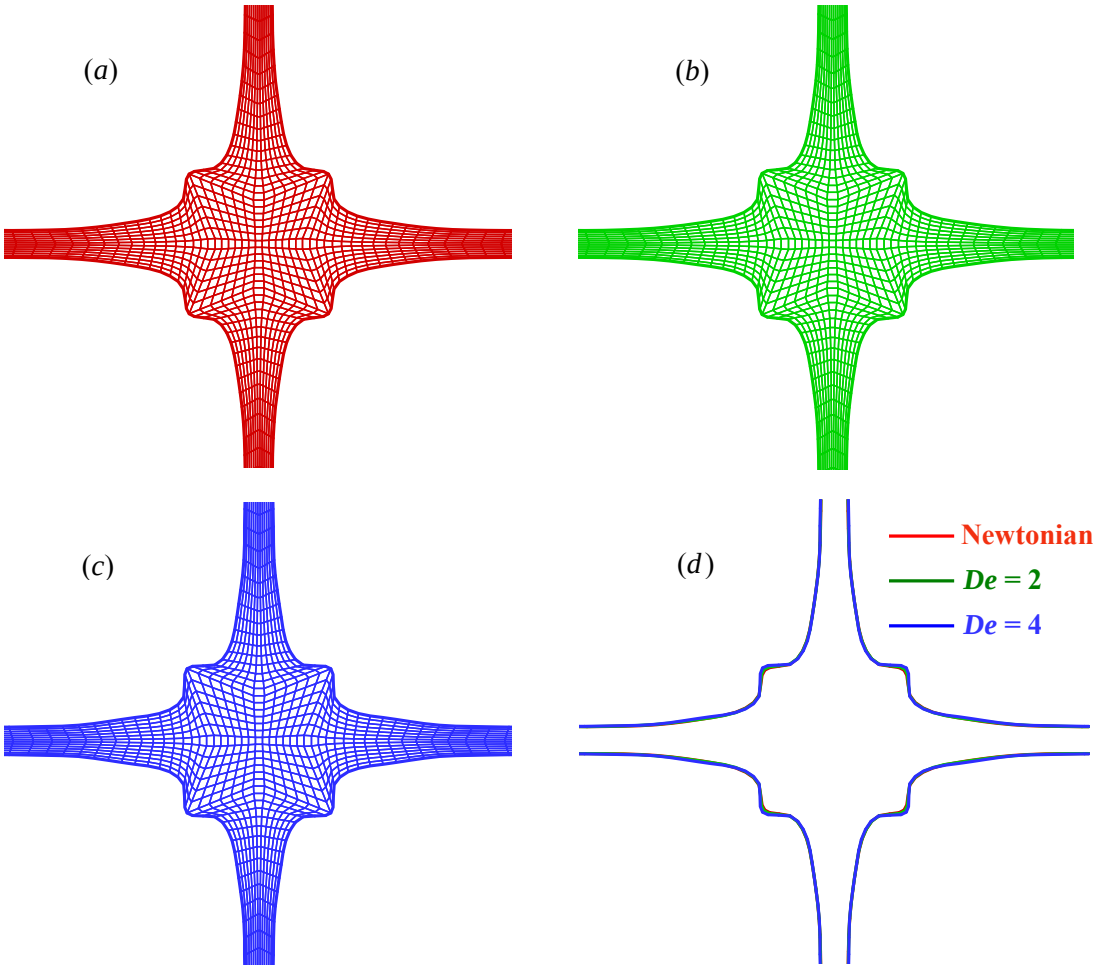

Fig.5. Optimized cross-slot flow geometries for (*a*) Newtonian flow and UCM fluid flow at (*b*) $De = 2$ ($Wi = 0.2$) and (*c*) $De = 4$ ($Wi = 0.4$). The shape of the optimized geometries is compared in part (*d*).

In Figure 5 we present the optimized cross-slot geometries for creeping flow of a Newtonian fluid and for an UCM fluid at two distinct *De* values. As shown in Figure 5 (*d*) the optimal shape is nearly insensitive to *De*, making it possible to obtain a universal cross-slot capable of generating an ideal planar extensional flow of

Newtonian and viscoelastic fluids at low Reynolds number. To quantify the elastic behavior, it is useful to define a Weissenberg number evaluated in the stagnation point region, $Wi = \lambda\dot{\varepsilon}$. From the target strain-rate profiles expressed through Eq. (3), it is easy to relate *Wi* and *De* as: $Wi = De/10$. As a result, for the UCM model the range of applicability of this extensional flow is restricted to $De < 5$, since the extensional viscosity becomes unbounded when $Wi \geq 0.5$ [21].

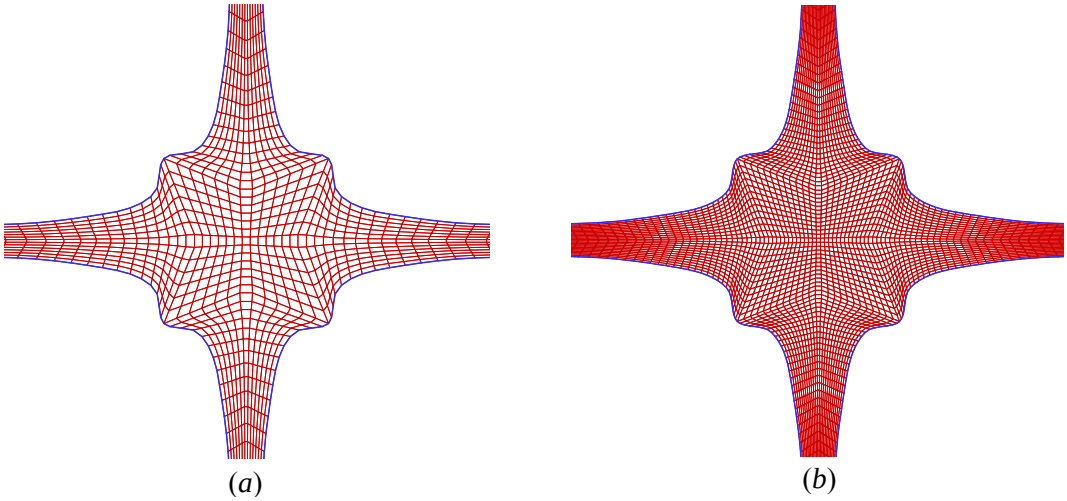

Fig.6. Comparison of the optimized cross-slot flow geometries calculated for Newtonian fluid flow using (*a*) mesh M1 and (*b*) mesh M2.

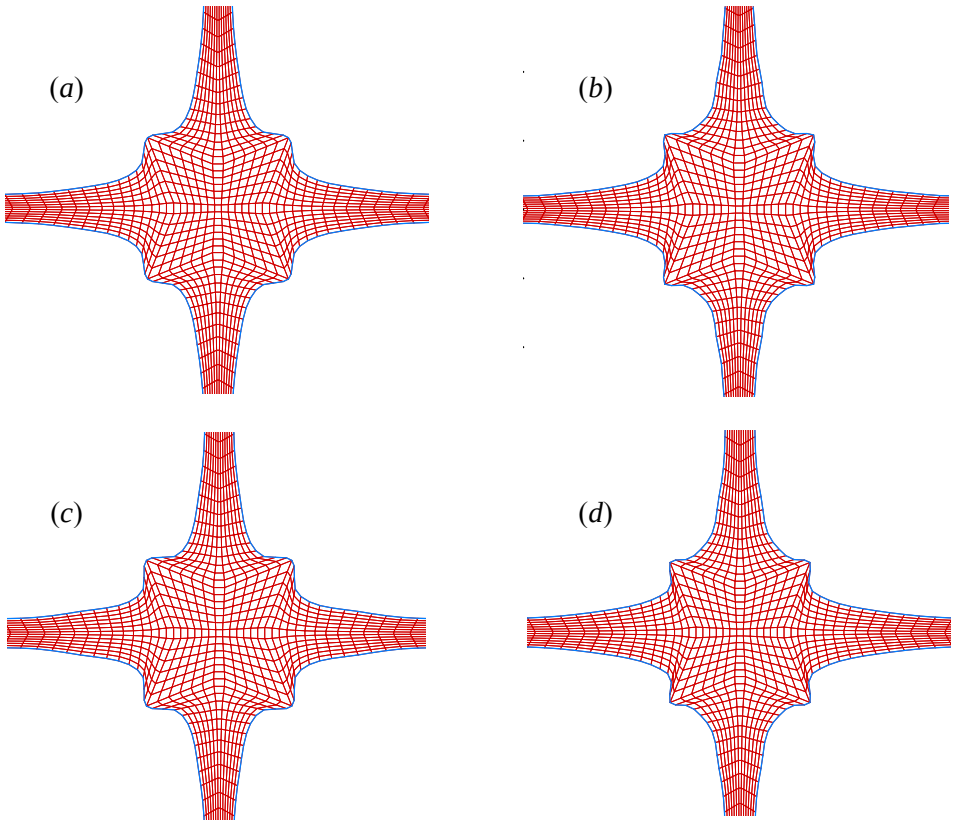

Fig.7. Comparison of the optimized cross-slot flow geometries for Newtonian and viscoelastic flow using mesh M1 and different dimensions of the search space: (*a*) $De = 0$, $N = 9$; (*b*) $De = 0$, $N = 19$; (*c*) $De = 4$, $N = 9$; (*d*) $De = 4$, $N = 19$.

In order to investigate the influence of mesh refinement in the computed solution, we have also performed the optimization cycle for the refined mesh (M2). In Figure 6 we compare the optimized geometry obtained with both meshes for the Newtonian fluid flow, thus demonstrating the accuracy of the results obtained with the

coarse mesh M1, which was the selected mesh for most of the optimization studies reported in this work. We note that most of the simulation time is spent on the evaluation of the objective function, which requires a full CFD simulation, therefore the computational time required to achieve the optimal geometry is directly proportional to the time spent in the flow simulation. As a result, the number of cells of the computational mesh should be reduced to a minimum, but without neglecting the accuracy of the CFD simulation.

The dimension of the search space, N, also influences the computed optimal solution. Increasing the number of variables will lead to a smoother and better solution, however the number of objective function evaluations required to achieve its minimum will increase significantly with N, thus this value should also be kept as low as possible. In Figure 7 we compare the solution obtained with the base case, $N = 9$, with the solution obtained with $N = 19$. Again, we observe that the base solution ($N = 9$) is very good, both for the Newtonian fluid and the UCM fluid at $De = 4$ ($Wi = 0.4$), therefore justifying the choice of this dimension of the search space in the remaining optimization studies.

In Figure 8 we present the streamwise velocity profile on the centerline along the y-direction for both the Newtonian and the De =4 cases. The target profile is reasonably well predicted, thus demonstrating that the optimization algorithm developed in this study performs well. In future works we will study different target profiles, defined in order to generate continuous strain-rate profiles. In those cases we expect better agreement between the optimized and the target profiles.

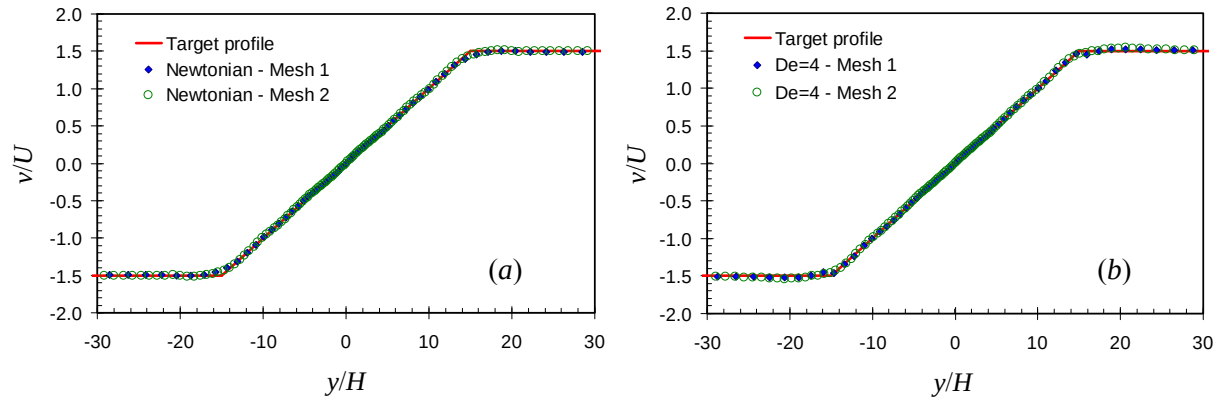

Fig.8. Velocity profiles along the y-axis for the optimized cross-slot flow geometries ($N = 9$). (a) Newtonian fluid; (b) UCM fluid at $De = 4$. Comparison between the results predicted with meshes M1 and M2 and the target profile.

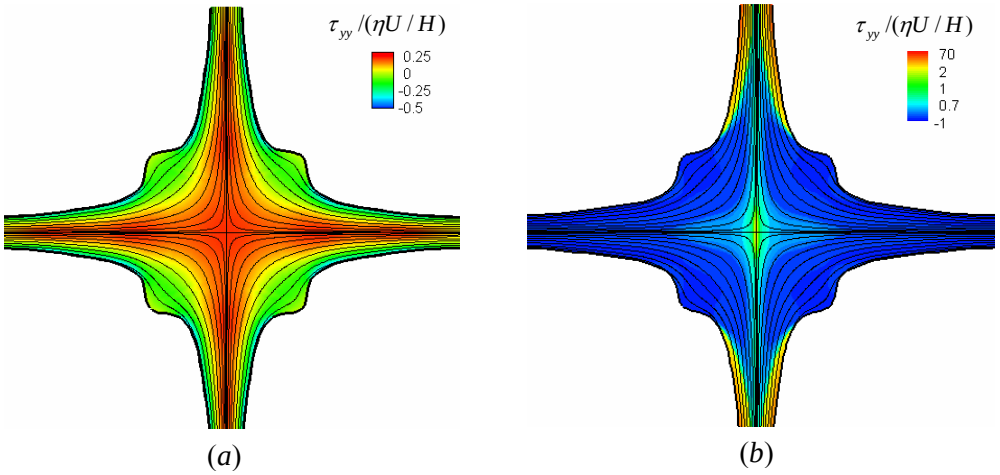

Fig.9. Predicted streamlines and contour plots of $\tau_{yy}/(\eta U/H)$ for the optimized cross-slot flow geometries. (a) Newtonian fluid; (b) UCM fluid at $De = 4$.

To conclude, in Figure 9 we present the predicted streamlines obtained in the optimized geometries for the Newtonian and De =4 cases. In both cases the streamline plots are similar; however, the stress fields are significantly different as illustrated in the contour plots of $\tau_{yy}/(\eta U/H)$ also illustrated in Figure 9. For the viscoelastic case the typical birefringence strand is observed along the y-direction, where the polymer molecules

are highly stretched generating very large normal stresses. We envisage the construction of a microfluidic apparatus with this type of configuration capable of measuring the extensional viscosity of dilute polymeric solutions from birefringence measurements.

4 Conclusions

An automatic algorithm for optimal shape design studies of viscoelastic fluid flow was developed. The methodology couples a finite-volume viscoelastic code [1] with the CONDOR optimizer [2] and a fully automated mesh generation and adaptation procedure. The optimization strategy was tested in the design of a cross-slot flow geometry in order to attain an ideal planar extensional flow. Despite the high payload in computing the objective function, which corresponds to a full CFD simulation, the numerical results show the reliability of the implemented optimization algorithm to perform these types of studies using Newtonian or viscoelastic fluids under low Reynolds number flows.

The microfluidic device designed was shown to achieve a quasi-homogeneous elongational flow, a crucial requirement to produce meaningful rheological measurements.

Acknowledgements

Financial support from FEDER and FCT through projects POCI/EQU/56342/2004 and PTDC/EQU-FTT/71800/2006 is gratefully acknowledged.

References

1. M.A. Alves, P. J. Oliveira and F. T. Pinho, A convergent and universally bounded interpolation scheme for the treatment of advection, *Int. J. Num. Meth. Fluids*, Vol. 41, pp. 47-75 (2003).
2. F.V. Berghen and H. Bersini, CONDOR, a new parallel, constrained extension of Powell's UOBYQA algorithm: Experimental results and comparison with the DFO algorithm, *J. Comp. Appl. Math*., Vol. 181, pp. 157-175 (2005).
3. B. Mohammadi, and O. Pironneau, Shape optimization in fluid mechanics, *Ann. Review Fluid Mech*., **36** (2004) 255-279.
4. A. Jameson, Aerodynamic design and optimization, *16th AIAA Comp. Fluid Dynamics Conf.*, AIAA Paper A-2003-3438, Orlando, FL, June 23-26 (2003).
5. F. Baron and O. Pironneau, Multidisciplinary optimal design of a wing prole, in *Structural Optimization 93, The world congress on optimal design of structural systems*, J. Herskovits (Ed.), Vol. 2, pp. 61-68, Rio de Janeiro, Brazil: UFRJ Press (1993).
6. G.W. Burgreen, J.F. Antaki, Z.J. Wu and A.J. Holmes, Computational Fluid Dynamics as a development tool for rotary blood pumps, *Artificial Organs*, Vol. 25, pp. 336-340 (2001).
7. Y. Tahara, S. Tohyama and T. Katsui, CFD-based multi-objective optimization method for ship design, *Int. J. Num. Meth. Fluids*, Vol. 52, pp. 499-527 (2006).
8. M.K. Karakasis, D.G. Koubogiannis and K.C. Giannakoglou, Hierarchical distributed metamodel-assisted evolutionary algorithms in shape optimization, *Int. J. Num. Meth. Fluids*, Vol. 53, pp. 455-469 (2007).
9. R. Makinen, J. Periaux and J. Toivanen, Multidisciplinary shape optimization in aerodynamics and electromagnetics using genetic algorithms, *Int. J. Numer. Meth. Fluids*, Vol. 30, pp. 149-159 (1999).
10. F.V. Berghen, CONDOR User's guide (document v.1.05), Internal Report, IRIDIA, Université Libre de Bruxelles), Belgium (2004).
11. F.V. Berghen, CONDOR: a constrained, non-linear, derivative-free parallel optimizer for continuous, high computing load, noisy objective functions, *PhD Thesis*, University of Brussels (ULB - Université Libre de Bruxelles), Belgium (2004).
12. M.J.D. Powell, UOBYQA: Unconstrained Optimization By Quadratic Approximation, Technical report (DAMTP2000/14), Department of Applied Mathematics and Theoretical Physics, University of Cambridge, England, (2000).
13. G.M. Whitesides, The origins and the future of microfluidics, *Nature*, Vol. 442, pp. 368-373 (2006).
14. H.A. Stone, A.D. Stroock and A. Ajdari, Engineering flows in small devices: Microfluidic toward a lab-on-a-chip, *Ann. Rev. Fluid Mech.*, Vol. 36, pp. 381-411 (2004).
15. L.E. Rodd, T.P. Scott, D.V. Boger, J.J. Cooper-White and G.H. McKinley, The inertio-elastic planar entry flow of low-viscosity elastic fluids in micro-fabricated geometries, *J. Non-Newt. Fluid Mech.*, Vol. 129, pp. 1-22 (2005).

16. L.E. Rodd, J.J. Cooper-White, G.H. McKinley and D.V. Boger, Role of the elasticity number in entry flow of dilute polymer solutions in microfabricated contraction geometries, *J. Non-Newt. Fluid Mech.*, Vol. 143, pp. 170-191 (2007).
17. P.J. Shrewsbury, and S.J. Muller, Effect of flow on complex biological macromolecules in microfluidic devices, *Biomedical Microdevices*, Vol.3, pp. 225-238 (2001).
18. A. Groisman and S.R. Quake, A microfluidic rectifier: anisotropic flow resistance at low Reynolds numbers, *Phys. Rev. Lett.*, Vol. 92:094501 (2004).
19. P.E. Arratia, C.C. Thomas, J. Diorio, and J. P. Gollub, Elastic instabilities of polymer solutions in cross-channel flow, *Phys. Rev. Lett.*, Vol. 96:144502 (2006).
20. J.M. Soulages, Flow birefringence and velocity measurements for polymer melts in a cross-slot flow channel, PhD Thesis, ETH Zürich, Nr. 17180 (2007).
21. R.G. Owens and T.N. Phillips, *Computational rheology*, Imperial College Press, London (2002).